



Quantifying vulnerability of Antarctic ice shelves to hydrofracture using microwave scattering properties



K.E. Alley^{a,*}, T.A. Scambos^a, J.Z. Miller^b, D.G. Long^c, M. MacFerrin^a

^a University of Colorado Boulder, 1540 30th St., RL-2 Room 201, Boulder, CO 80303, USA

^b Byrd Polar Research Center, Ohio State University, 108 Scott Hall, 1090 Carmack Rd., Columbus, OH 43210, USA

^c 459 CB, Brigham Young University, Provo, UT 84602, USA

ARTICLE INFO

Keywords:

Glaciology
Antarctica
Ice shelves
Scatterometry
QuikSCAT

ABSTRACT

Recent ice shelf disintegrations on the Antarctic Peninsula and subsequent increases in ice sheet mass loss have highlighted the importance of tracking ice shelf stability with respect to surface melt ponding and hydrofracture. In this study, we use active microwave scatterometry in time-series to estimate melt season duration, and winter backscatter levels as a proxy for relative concentration of refrozen ice lenses in Antarctic ice shelf firn. We demonstrate a physical relationship between melt days and firn/ice backscatter using scatterometry and field data from Greenland, and apply the observed relationship to derive and map a vulnerability index for Antarctica's ice shelves. The index reveals that some remaining Antarctic Peninsula ice shelves have already reached a firn state that is vulnerable to hydrofracture. We also show that the progression of an ice shelf towards vulnerability is affected by many factors, such as surface mass balance, internal stresses, and ice shelf geometry.

1. Introduction

Atmospheric warming can lead to ice shelf disintegration through hydrofracture (Scambos et al., 2000, 2003; Rott et al., 1996; Hughes, 1983). Hydrofracture on glaciers and ice shelves occurs when water infiltrates crevasses, filling them to a level at which water pressure at the crack tip exceeds the fracture toughness of the ice as well as any compressive stresses transverse to the fracture orientation. For the fracture to continue to propagate, the crevasse tip pressure must continue to increase to offset increasing lithostatic pressure. This is facilitated by a surface reservoir of water that drains into the propagating fracture. Ponding of meltwater on the surface of ice shelves is an effective reservoir for hydrofracture. With closely-spaced fractures, fractured blocks may then topple, initiating a runaway disintegration effect (MacAyeal et al., 2003). This mechanism likely caused the complete or partial collapse of several ice shelves on the Antarctic Peninsula, including the rapid disintegration of the Larsen B Ice Shelf in 2002 (Scambos et al., 2003).

Not all ice shelves are vulnerable to hydrofracture. In regions with high winter snow accumulation or permeable, porous firn, any meltwater produced during summer months percolates into the upper firn and refreezes. To support surface ponds that provide the necessary water reservoir to initiate hydrofracture, the firn layer must be sufficiently saturated with refrozen meltwater to prevent efficient

downward percolation. Modeling studies and observations confirm that ice shelves that have collapsed on the Antarctic Peninsula in the past had very little firn air thickness preceding disintegration, indicating that they were preconditioned for the hydrofracture mechanism to operate (Holland et al., 2011; Berthier et al., 2012; Kuipers Munneke et al., 2014).

Scambos et al. (2003) performed a pilot study investigating the utility of active microwave scatterometry for assessing ice shelf vulnerability to hydrofracture by analyzing the relative concentration of refrozen meltwater in firn layers. Using selected areas from several ice shelves, they demonstrated a predictable relationship between winter backscatter and ice shelf melt season duration. They interpreted this relationship as reflecting the ice-saturation state of the firn layer, based on a study linking radar scattering and ice sheet facies in Greenland (Fahnestock et al., 1993). On most shelves, backscatter increases with average annual melt days, because small ice lenses and other discontinuous refrozen structures are efficient diffuse scatterers. However, at high numbers of melt days, when ice lenses form large, nearly-continuous, and relatively smooth layers in the firn, specular reflections direct the microwave signal away from the sensor and backscatter values decrease (Fahnestock et al., 1993). As large, continuous ice lenses also impede meltwater percolation, promoting melt pond formation, shelf areas with lowered backscatter values at high numbers of annual melt days are inferred to be the areas most susceptible to hydrofracture

* Corresponding author at: 1540 30th St., RL-2 Room 201, Boulder, CO 80303, USA.

E-mail addresses: karen.alley@colorado.edu (K.E. Alley), teds@nsidc.org (T.A. Scambos), long@ee.byu.edu (D.G. Long), michael.macferrin@colorado.edu (M. MacFerrin).

(Scambos et al., 2003).

In this study, we use gridded scatterometry data to assess the relative concentration of refrozen meltwater in the firn (“firn-ice concentration”) for all Antarctic ice shelves. We assess this by examining the relationship between annual melt days and average winter backscatter. After introducing the data (Section 2), we demonstrate the relationship using scatterometry, ground-penetrating radar, and shallow firn cores in Greenland, where ice sheet facies are relatively well-mapped, and where their effect on surface meltwater ponding is well-known (Section 3). We then show that the melt days-backscatter relationship is similar for Antarctica’s ice shelves, and analyze the impacts of surface mass balance on this relationship (Section 4). Finally, in Section 5 we present our results, which comprise an index that assesses ice shelf vulnerability to surface-melt-induced hydrofracture collapse. Section 6 discusses the details of the index and the implications of our assessment.

2. Data

The backscatter data used in this study come from four sensors: the C-band (5.7 cm wavelength) scatterometers ESCAT onboard the European Space Agency’s Earth Remote Sensing (ERS) satellites 1 (operational 1990–1995) and 2 (1995–1999); NASA’s Ku-band (2.2 cm wavelength) Seawinds instrument on the QuikSCAT satellite (2000–2009); and Eumetsat’s C-band Advanced Scatterometer (ASCAT) aboard the MetOp-A satellite (2007–present). All scatterometry data were obtained through Brigham Young University’s Microwave Earth Remote Sensing Laboratory Scatterometer Climate Record Pathfinder. We restricted our backscatter data analysis to austral winter months (June, July, and August) in order to avoid liquid meltwater, which significantly lowers backscatter values (Long and Drinkwater, 1994).

All backscatter data were processed using the Scatterometer Image Reconstruction (SIR) algorithm (Long et al., 1993), which uses multiple days of scatterometry data to create gridded, resolution-enhanced products. The algorithm assumes a linear model that relates the normalized radar cross-section, σ^0 , which is measured in decibels, and the signal incidence angle:

$$\sigma^0 = A + B(\theta - 40)$$

The model normalizes the incidence angle to 40°. This creates two images: an A image, which contains the normalized backscatter values and has units of dB, and a B image, which represents the dependence of backscatter on incidence angle and has units of dB/°. In this study, we utilize the A images.

When applied to ERS data, the algorithm combines passes from multiple orbits, which requires the assumption that backscatter is independent of azimuth. Products are provided on a 25 km grid, with an estimated effective resolution of 25–30 km. ERS images are obtained using a vertically polarized microwave signal. In this study, the subset of data between 1991 and 1996 were used, a time period that includes maximum coverage consistency in the available data.

C-band ASCAT data were obtained for both Greenland and Antarctica for the time period 2009–2013. These images also combine multiple passes, and are vertically polarized. Data are provided on 4.45 km grids, with an estimated resolution of 12–15 km. In this study, ASCAT data were down-sampled (via spatial averaging) to match the 25 km resolution of passive-microwave melt-days datasets. Ku-band QuikSCAT data are available from 2000 to 2009 as a variety of products, including both vertical and horizontal polarization, and also combine multiple passes. Data are provided on a 4.45 km grid, with an effective resolution of 8–10 km. QuikSCAT data were kept on the original 4.45 km grid for this study.

We used 10-year averages of passive microwave surface melt products for Greenland and Antarctica to document annual melt days for the periods leading up to the ASCAT and ERS datasets (Mote, 2014; Picard and Fily, 2006). We chose this time scale to establish a relatively

long-term average while avoiding biases from melt season effects buried below scatterometer penetration depths. We also created a third, higher-resolution dataset for Antarctic surface melt derived from ten years of available QuikSCAT backscatter data, following the technique presented in Hicks and Long (2011).

Additional validation data for the subsurface physical processes that drive the backscatter-melt days relationship come from ground-penetrating radar and shallow firn cores. These data were collected during a field campaign in southwest Greenland in the spring of 2013 (Machguth et al., 2016).

All Antarctic data were provided as continent-wide datasets. Subsetting of ice shelf regions was carried out using the MODIS Mosaic of Antarctica (MOA) 2009-derived coastline and grounding line (Scambos et al., 2007; Haran et al., 2014). Modifications were made to the outlines of the Ross and Filchner-Ronne ice shelves for ERS-1 and -2 to exclude large no-data regions near the pole.

3. Backscatter/melt days relationship development and validation

The physical relationship presented by Scambos et al. (2003) is essentially a microwave-based documentation of snow facies for Antarctic ice shelves. The observed categories are more easily identified and described in Greenland. Benson (1962) divided the Greenland ice sheet into four snow facies (dry snow, percolation, wet snow, and bare ice zones) based on their physical characteristics using in situ summer observations. Fahnestock et al. (1993) observed these same facies using winter SAR backscatter and discussed the physical features causing the distinctive backscatter response. Similar results have been presented in other studies (e.g. Jezek et al., 1993; Long and Drinkwater, 1994).

At the highest elevations in Greenland, in the dry snow zone, little or no melt occurs throughout the year, and backscatter values are typically very low due to penetration and absorption of microwave energy in the firn. At slightly lower elevations, in the percolation zone, summer melt is more intense and cooler subsurface temperatures cause meltwater to refreeze within the firn column, forming small, discontinuous ice lenses and pipes. These are efficient scatterers of microwave energy (Jezek et al., 1994; Partington, 1998; Hall et al., 2000; Haas et al., 2001; Willmes et al., 2011), and as summer melt intensity increases (with decreasing elevation on the ice sheet, among other factors), the winter backscatter signal rises. At lower elevations, in the wet snow zone, the entire upper firn column is wetted by melt and refreezes in winter to form large ice lenses, or (lower still) a nearly uniform near-surface ice layer in the superimposed ice zone. The bare ice zone at the lowest elevations is formed where summer melt removes the entire winter snow column and firn layer, leaving smooth glacial ice at the surface. In contrast to the increasing backscatter values with decreasing elevation observed through the percolation zone, the low-elevation shift found in the superimposed ice and bare ice zones to large, continuous layers of ice creates a specular surface for microwave radiation, buried under dry snow in winter. Specular reflections redirect the active microwave signal primarily away from the sensor, causing a decrease in measured backscatter. Therefore, overall we expect a graph of winter backscatter vs. average annual melt days to show increasing backscatter with increasing melt days, until some threshold where backscatter values decrease due to specular reflections at high numbers of annual melt days.

We infer that similar processes affect the firn column on Antarctic ice shelves, with analogous effects on backscatter. Cool-summer ice shelf areas have no significant summer melting, analogous to the dry snow zone in Greenland. Some areas receive a little melt, and have small, discontinuous ice lenses in the firn, similar to Greenland’s percolation zone. A few areas receive significant amounts of melt that lead to the formation of superimposed ice capable of specular reflection of microwave energy. However, unlike in Greenland, where summer melt intensity is strongly correlated with elevation, snow facies on Antarctic ice shelves are more closely tied to local summer climate, and vary

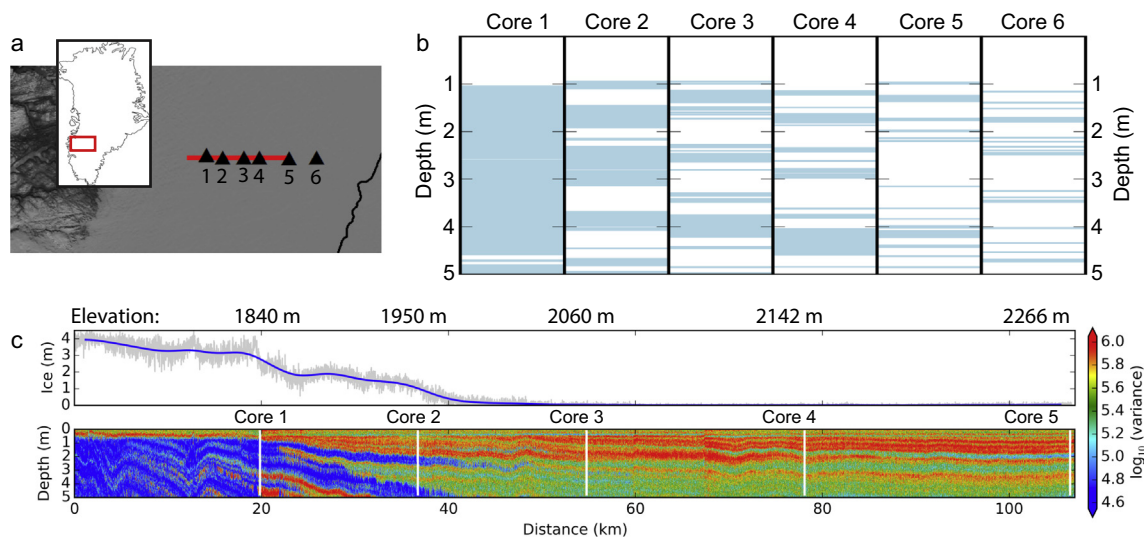


Fig. 1. a) Data collection locations for spring 2013 field campaign. Core locations shown as black triangles; radar transect shown in red. b) Ice lenses (blue) in the top five meters of firn cores; collection locations shown as black triangles in (a). c) Ground-penetrating radar transect (bottom) showing thickness of large ice lenses (~ 0.8 m, top). Radar transect location shown in red in (a); distance along transect goes from east to west. (For interpretation of the references to color in this figure legend, the reader is referred to the web version of this article.)

spatially around the continent (Trusel et al., 2012). This makes it difficult to validate the physical relationship on Antarctic ice shelves, where continuous samples including all ice facies cannot be readily identified.

Therefore, to explore the physical relationship between ice lens content and backscatter, we extracted data sets for mean backscatter and mean summer melt days for two transects across southwestern Greenland that together span all snow/firn facies. One of these transects coincides with field data from a spring 2013 field campaign (Fig. 1) investigating the ice layer content of the firn in the transition from the percolation zone to the superimposed ice zone (Machguth et al., 2016). Fig. 1b shows ice lenses in the top 5 m of firn as observed in an uphill series of shallow firn cores. Fig. 1c shows the cumulative thickness of large ice lenses (top) derived from a GPR transect (bottom) spanning the same region. We collected the GPR data with an 800 MHz shielded Tx/Rx antenna from Malå Geosciences. After data collection, we combined the raw radar traces to form a continuous transect, resampled traces for constant 1.5 m horizontal spacing, pre-processed the data using a high-pass filter with a time window of 1.25 ns (\sim one radar wavelength), and used a 3×13 moving window to determine the local variance of each sample, as described in detail by Machguth et al. (2016). The GPR signal contains more scatter in regions of porous firn than in volumes of solid ice, and the log-transform of local signal variance shows distinct patterns that correlate very well with ice lenses in coincident cores. Log-variance values of 4.75 or less (blue regions of the GPR plot) correlate best with thick ice lenses retrieved from coincident cores (Machguth et al., 2016). The resolution of the radar signal and the post-processing enhancement allow us to detect thick ($> \sim 0.8$ m vertical) and continuous ($> \sim 20$ m horizontal) ice lenses, while thinner lenses (such as those seen in cores #3–6, Fig. 1b) are generally unresolved.

The field data in Fig. 1 show a predictable gradient in ice lens content based on climatic gradients due mainly to elevation in this region. Firn at the lowest elevations is nearly completely ice-saturated with thick, continuous ice lenses. These lenses are thinner and less extensive at higher elevation sites. However, even the highest-elevation cores in this region exhibit significant ice lens presence, a characteristic we expect to see represented in backscatter data.

Fig. 2 shows extracted backscatter and average annual melt days values for a 100 km-wide transect from the central ice divide downhill to the coast (red), which is coincident with the field data in Fig. 1.

Because the highest point on this transect is already within the percolation zone, we also extracted a transect (blue) from Greenland's Summit Station, well within the dry snow zone, downhill to Kangerlussuaq in the bare ice zone (Benson, 1962; Fahnestock et al., 1993), including all four ice facies following the elevation gradient. Average annual melt days are derived from passive microwave data (Mote, 2014), and backscatter values are from ASCAT. The data from the two transects closely overlap when graphed, indicating that the firn layer exhibits the same progression of ice lenses within each transect.

The resulting graph of backscatter vs. melt days illustrated by both transects (Fig. 2b) reveals a curve with a very distinctive shape, a relationship described earlier based on satellite radar backscatter mapping of the progression of snow facies (Fahnestock et al., 1993). Progression up the trend with increasing backscatter and melt days (which is approximately the same as progression downward in elevation) is accompanied by an increase in ice lenses in the firn that ultimately leads to surface-supported meltwater features. The decrease in backscatter at high melt, representing a shift towards increased specular reflection, occurs at slightly fewer melt days than the zone where GPR data and firn cores begin to show a significant fraction of large ice lenses, and where surface meltwater accumulations are typically visible in summer. This difference is attributed to discrepancies between the onset of ice layer specularity to microwaves (in the frequency band of the respective sensors) and the point at which ice layers are extensive and thick enough to support meltwater. As noted, the GPR data were processed to detect ice lenses $> \sim 0.8$ m thick, but as specular reflections are primarily a surface scattering response (Carsey, 1992), reduced backscatter should be observable with the much thinner, yet widespread, ice lenses observed in the firn cores above the superimposed ice zone. The thickest ice lenses near the surface in Core 5, close to the decrease in backscatter, are 25 cm or less. In addition, our goal is an assessment of the *potential* for ponded melt on the firn surface, a key precursor to hydrofracture in both Greenland and Antarctica. To achieve this, we need to evaluate the threshold of specularity in firn as an indication of surpassing a state close to, but not at, the point of supporting an accumulation of meltwater above the ice layer. In our Greenland validation site, this threshold where specular reflectivity of ASCAT scatterometry begins to dominate the return signal strength above ~ 20 melt days.

Based on the field evidence from southwest Greenland shown in Fig. 1, we know that significant amounts of summer meltwater are

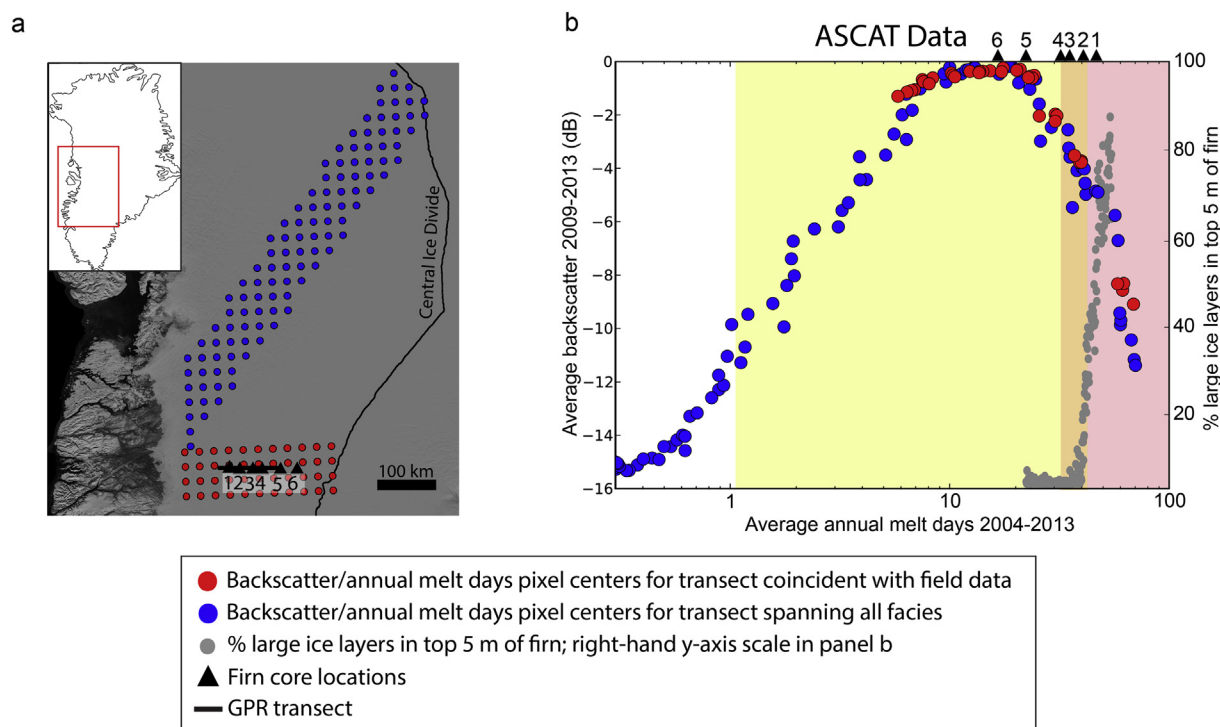


Fig. 2. Backscatterer/melt days relationship in Greenland. a) Pixel center locations for transects from Summit Station to Kangerlussuaq (blue dots) and Greenland's central ice divide to the ice edge (red dots). b) Blue and red dots correspond to transects in (a). Backscatter data are from ASCAT, melt days data are from Mote (2014). Yellow shading represents the percolation zone, orange is deep percolation (Machguth et al., 2016), and red is the runoff zone observed in 2013. (For interpretation of the references to color in this figure legend, the reader is referred to the web version of this article.)

supported (perched) above ice layers in the deep percolation zone in summer (orange shading in Fig. 2b), at least temporarily (Machguth et al., 2016; Humphrey et al., 2012). The deep percolation zone correlates with a melt day frequency of approximately 35 days. Thus, we can infer that significant surface or near-surface melt retention along this transect begins to occur in areas where melt day frequency exceeds ~ 1.6 times the point at which specular reflection in the firn layer begins, as measured by ASCAT. This ratio will differ depending on the sensor frequency, surface melt intensity, and surface accumulation rate, which we discuss further in Section 4. The precise implications of the specular reflection threshold of hydrofracture vulnerability therefore vary based on location; nonetheless, it corresponds to widespread re-frozen ice lenses in the firn, which is a physically based determination of the ice areas most vulnerable to hydrofracture.

As noted, the penetration depth of the sensor is an important factor affecting the point at which the specular reflection threshold is reached. ASCAT is a C-band microwave instrument. Estimates for C-band penetration depths vary widely in polar firn (for example, Rott et al. (1993) estimated a penetration depth of ~ 10 m in dry snow; Bingham and Drinkwater (2000) showed penetration depths from ~ 1 m to > 100 m depending on snow grain size; Rignot et al. (2001) concluded that C-band InSAR can penetrate up to 10 m in cold, dry firn. All of these studies agree that a smaller grain size or the presence of liquid water decreases penetration depth). In this study, the backscatter data are limited to the winter season when very little liquid water is present. Therefore, regardless of the assumed C-band penetration depth, ASCAT should be sensitive to extensive ice layers that are formed deep enough that more porous firn above the layer could store meltwater during summer and prevent visible ponding.

In following sections we utilize the Ku-band instrument QuikSCAT for our Antarctic analysis because it has a much lower penetration depth (Rott et al., 1993) and therefore responds to lenses that are closer to the surface. However, it would not be reasonable to compare QuikSCAT data to 2013 field data in Greenland, because QuikSCAT

failed before the anomalously large 2012 melt event that significantly impacted the field data (Machguth et al., 2016). We show in the next section that the physical relationship, represented by the distinctive graph shape from the Greenland data, is also present in the shapes of the curves in Antarctica, regardless of sensor, band, or time period. This consistency, along with the fundamentally relative nature of our vulnerability index, allows us to utilize QuikSCAT data for Antarctic analysis of hydrofracture susceptibility.

4. Backscatterer/melt days relationship in Antarctica

We expect to see the same backscatter response to ice lenses displayed by the distinct shape of the Greenland relationship in our analysis of Antarctic ice shelves. Fig. 3 explores the relationship using data from all Antarctic ice shelves, with region-average values displayed in 3a providing a broad indication of where various geographic areas fall on the facies progression. Individual ice shelf averages are provided in supplementary Fig. S1, and regional plots are provided in supplementary Figs. S2–S10. Despite a significant amount of scatter in the raw data (grey in Fig. 3c–e), backscatter values averaged within integer melt day bins (black in Fig. 3c–e) reveal a shape similar to that shown by our Greenland analysis. All scatterometry datasets considered show generally increasing backscatter with increasing melt days, and a clear decrease in backscatter at high melt day values.

Differences between sensors and detection bands cause backscatter values to vary between the Antarctica plots in Fig. 3. We also note that the specularity thresholds in the Antarctic data for all three sensors occur at higher numbers of annual melt days than the threshold in Greenland. In the case of Ku-band QuikSCAT, this is due in part to the lower penetration depth, requiring a greater degree of firn-ice saturation before specular behavior is achieved. Moreover, the melt intensity for an average melt day is likely to be lower for regions at higher latitude (south latitude) relative to the Greenland study. High melt intensities, such as those found in Greenland, yield low melt-day

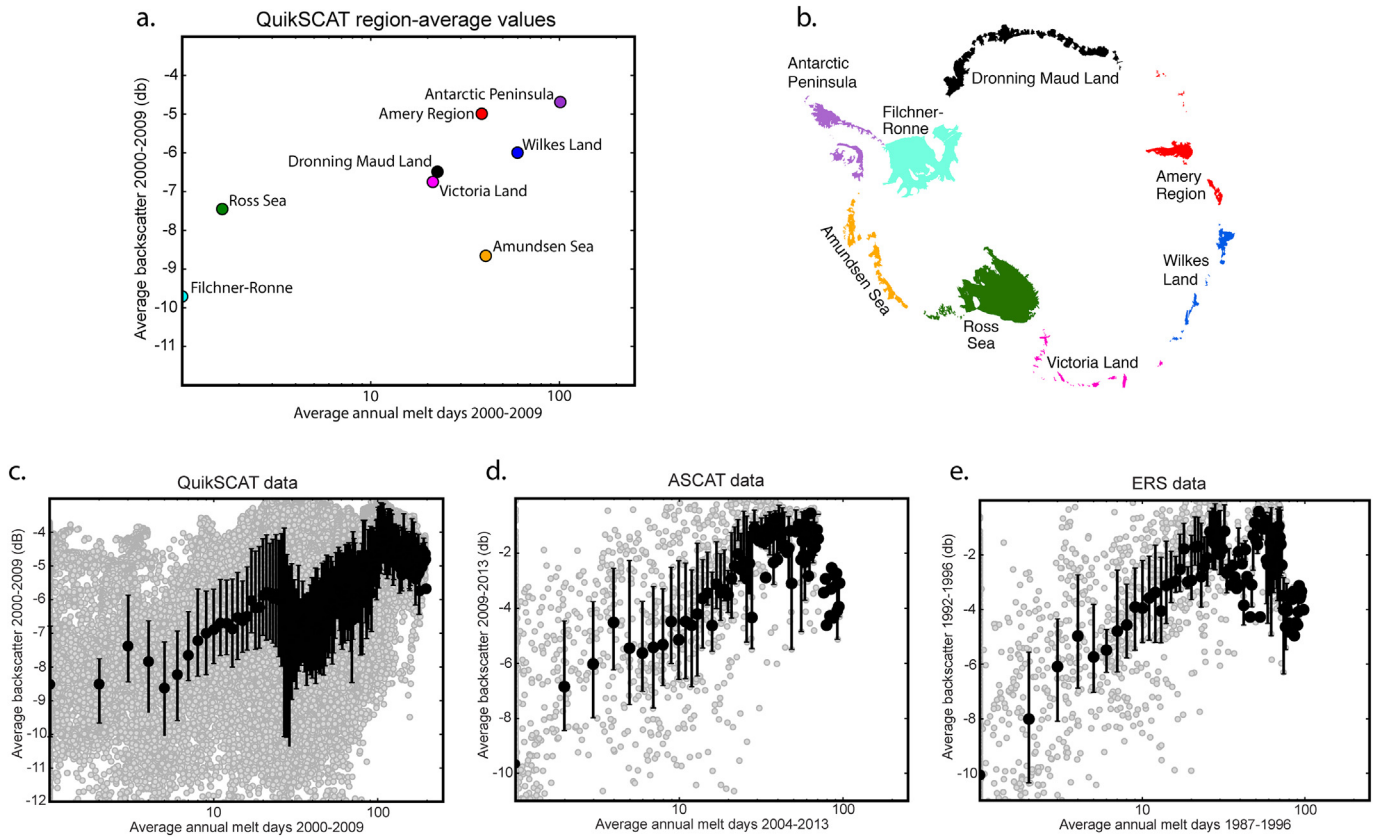


Fig. 3. Backscatter/melt days relationship in Antarctica. a) Region-average values for all Antarctic ice shelves, with colors corresponding to regions shown in b. Both melt day count and backscatter are derived from QuikSCAT. Related plots in supplementary Figs. S4–S11. c) Same data used in a, binned and averaged by integer melt day (black) and shown without averaging (grey). d) Same as c, but with backscatter from ASCAT and melt days from ten years of passive microwave data overlapping the ASCAT data used (Picard and Fily, 2006). e) Same as d, but with backscatter from ERS, and melt days from ten years of passive microwave data overlapping the ERS data acquisition period. Error bars in c–e show the central 50% of the raw data distribution.

thresholds for the shift to specular reflection characteristics, while lower melt intensities in Antarctica yield higher specular reflection thresholds. Therefore, absolute variable values are not directly comparable between plots, but the shared physical relationship makes the shapes of the plots directly analogous. Fig. 2 demonstrates the expected graph shape using data that cross the full range of firm saturation states; Fig. 3 demonstrates that, regardless of sensor, band or time period, the same processes and range of firm states are evident in the shapes of the graphs derived from all Antarctic ice shelf data. Therefore, the decrease in backscatter at high melt days is a reliable relative indicator of a high degree of firm-ice saturation, which makes the ice area more vulnerable to hydrofracture.

We continue our analysis exclusively using QuikSCAT data, because it has a long continuous record that allows for the extraction of a continuous annual melt days record directly from backscatter products that have a much higher spatial resolution than passive microwave melt day datasets. Consequently, the QuikSCAT analyses and maps can be produced at a much higher spatial resolution than those produced from ERS or ASCAT data.

As noted previously, the grey points in Fig. 3c–e show a large amount of scatter in the raw data. Fig. 4 shows that much of the scatter found in the raw QuikSCAT data may be explained by differences in surface mass balance over ice shelf areas that experience the same number of annual melt days. Using surface mass balances from RACMO2.3 (Van Wessem et al., 2014), we separated the data into three surface mass balance categories. Ice shelves in a low surface mass balance category exhibit higher backscatter for each annual melt days value, and the drop in backscatter representing specular reflection is reached at a lower number of melt days than in the higher mass balance categories (in the highest mass balance category, the drop in

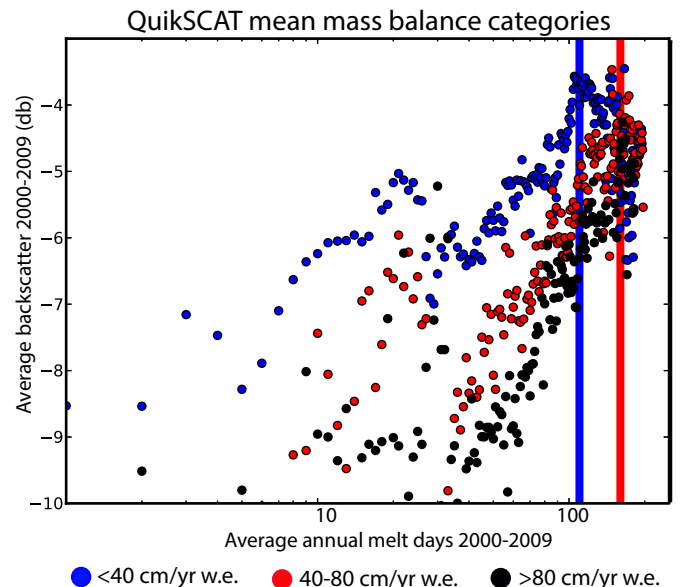


Fig. 4. Backscatter/melt days relationship for QuikSCAT, with data separated by surface mass balance category (Van Wessem et al., 2014) and averaged per integer melt day. Surface mass balance categories are in cm/yr water equivalent (w.e.). Blue vertical line marks the decrease in backscatter at high annual melt days in the lowest surface mass balance category; red vertical line corresponds to the decrease in the middle surface mass balance category. No decrease in backscatter was observed in the highest surface mass balance category. (For interpretation of the references to color in this figure legend, the reader is referred to the web version of this article.)

backscatter is not present). Because the backscatter decrease is caused by the saturation-state of the firn with refrozen meltwater, this threshold, and the overall backscatter/melt days relationship, is determined in part by the ratio between annual surface melt and accumulation rate (Pfeffer et al., 1991; Braithwaite et al., 1994). Ice shelves that receive large amounts of snowfall, for example, must experience more melt to fill the air space being replenished each year.

We further demonstrated the relationship between accumulation rate and firn ice lens content (or, conversely, firn air content (Pfeffer et al., 1991; Braithwaite et al., 1994)) shown in Fig. 4 by performing statistical correlations between surface mass balance and backscatter within sub-datasets that have pixels with the same integer number of average annual melt days. The results are very similar to what would be achieved using multiple linear regression, but apply better to the non-linear nature of the total backscatter/melt days relationship.

First, we grouped the backscatter and accumulation values that correspond to pixels that experience each integer melt day value. For example, all pixels that experience a rounded 1 melt day per year are placed in a single category. Then, any array comprising less than thirty pixels was removed because these would not yield robust statistical results. This left 137 integer melt day categories. Within each category, we performed a Spearman's correlation between backscatter and accumulation. Of the 137 categories, 100 had a significant negative correlation at the 95% confidence level, meaning that higher surface mass balance rates are associated with lower backscatter values for pixels that experience approximately the same amount of melt each year. This result supports the graphical evidence in Fig. 4 that differences in surface mass balance cause divergence in backscatter values that appear as random scatter in the raw data.

Backscatter values are also affected by other variables relevant to the Antarctic ice sheet. For example, heavily crevassed regions may create anomalously high backscatter values for a given number of annual melt days. Mixed pixels near ice-rock or ice-ocean interfaces can similarly introduce error. We did not attempt to mask these areas in our study; they comprise only a small fraction of the shelf areas, and the similarity between the shapes of the average Antarctic curve and the well-constrained Greenland curve indicate that they do not strongly influence the averages. Another factor that might add scatter to the relationship is the presence of firn aquifers, which hold liquid water year-round (Forster et al., 2013). In addition, strong prevailing winds create sastrugi in many locations on the Antarctic Ice Sheet surface, causing anisotropy of microwave signals. Analyses of C-band scatterometry show these effects to be generally small on ice shelves (Fraser et al., 2014). Again, the consistency in the shapes of the graphs show that these effects are not significantly biasing our results; however, they may be contributing to the scatter in the raw data. Further analysis would be required to assess the magnitude of the impacts of these and other factors.

5. Development of vulnerability index and error estimation

We use the mean relationships present in the QuikSCAT mass balance categories (Fig. 4) to create a relative index that shows ice shelf vulnerability to surface-melt-induced collapse via hydrofracture. The mapped index is shown in Fig. 5. The index relies upon the assumption that the ice shelf backscatter/melt days relationship represents the temporal evolution that an ice shelf might experience under changing climate conditions (the 'space for time' substitution), and that any ice shelf may evolve to higher/lower positions on this relationship if temperatures in Antarctica warm/cool.

Two different approaches are used simultaneously to create this index. First, ice shelf areas with high annual melt days and low backscatter are classified as vulnerable to collapse, as the reduced backscatter observed indicates a significantly ice-saturated firn layer that could support melt ponding. For the QuikSCAT data, the selected threshold is at 119 average annual melt days in the lowest surface mass

balance category, and 185 in the middle category (thresholds shown as blue and red vertical lines in Fig. 4). These thresholds were determined by fitting a quadratic curve to the upper half of the averaged backscatter/melt days relationship and identifying the peak in the lower two mass balance categories; the data in the highest mass balance category do not exhibit a thresholding behavior. Because there are relatively few data points above the determined thresholds and rigorous ground-truthing data are not available, it is difficult to distinguish sub-categories above the specularly thresholds in the backscatter/melt days data. Therefore, we group all of these points into the same category, and use the term "significantly ice-saturated" to indicate the presence of large, continuous ice layers. We remove these points for the rest of the analysis, which exploits the approximately linear relationship present in the remaining data when plotted on log scales. Second, after data points above the thresholds are removed, we carry out a simple, two-dimensional principal component analysis within each mass balance category, which places an axis (the first principal component, supplementary Fig. S11) along the direction of maximum variability, weighting information from both the backscatter and melt days data. The index is created by projecting each pixel to its location along the first principal component axis, which represents a complete range of ice shelf facies from areas that experience no melt (and therefore have no refrozen ice lenses in the firn), to areas with significant summer melt that has led to nearly continuous refrozen ice layers. We then linearly scaled the values between zero and one, so that the index may be more easily read and interpreted. This pins zero at zero melt days and one at the calculated uppermost threshold within each category (or the highest value in the highest mass-balance category). Note that we reference these values and thresholds relative to annual melt days, but the values are really determined by equally weighting information from both melt days and backscatter data; we could not carry out the analysis without both datasets. Points that plot above one are areas with significantly ice-saturated firn, with large enough continuous ice layers to cause specular reflections of the microwave signal. Our result is a relative ranking of ice shelf vulnerability to hydrofracture, which indicates which ice shelves are closest to a firn condition that could support melt ponding, without explicit dependence on absolute backscatter or annual melt day values.

As shown in the graphs in Fig. 3, the non-averaged relationship between backscatter and annual melt days contains a large amount of scatter, and we wanted to get a sense of how this scatter introduces variability into the outcome of our mapped index. Because principal component analysis inherently reduces the two-dimensional relationship to one variable, quantification of variability must be performed along the principal component axis, rather than across an axis where a simple calculation of standard deviation would be relevant. In addition, variability quantification must account for the differing thresholds used in the surface mass balance categories.

Due to these limitations, we chose an empirical Monte Carlo-type simulation to assess the impacts of data scatter on the calculated vulnerability index. For 100 iterations within each surface mass balance category, we built a vulnerability index with a small but significant percentage (10%) of the data points removed. This random removal of different sets of points essentially allows us to quantify the effects of outliers on our results, while ensuring that we keep the full range of ice facies in our data, as is required for our analysis. For the lower two mass balance categories, we fit a quadratic function to the upper half of the data, which we used to identify a peak that was considered to be the ice-saturation threshold. The data for each iteration were then transformed to a vulnerability index as described above. Our process yielded 100 maps of ice shelf vulnerability to hydrofracture, which allowed us to calculate the standard deviation in the index value for each pixel in the map, as well as the standard deviation of the threshold values for those 100 iterations. Finally, we created maps of upper and lower estimates for the vulnerability index, which are equal to our best estimate for the index plus or minus two standard deviations as determined by

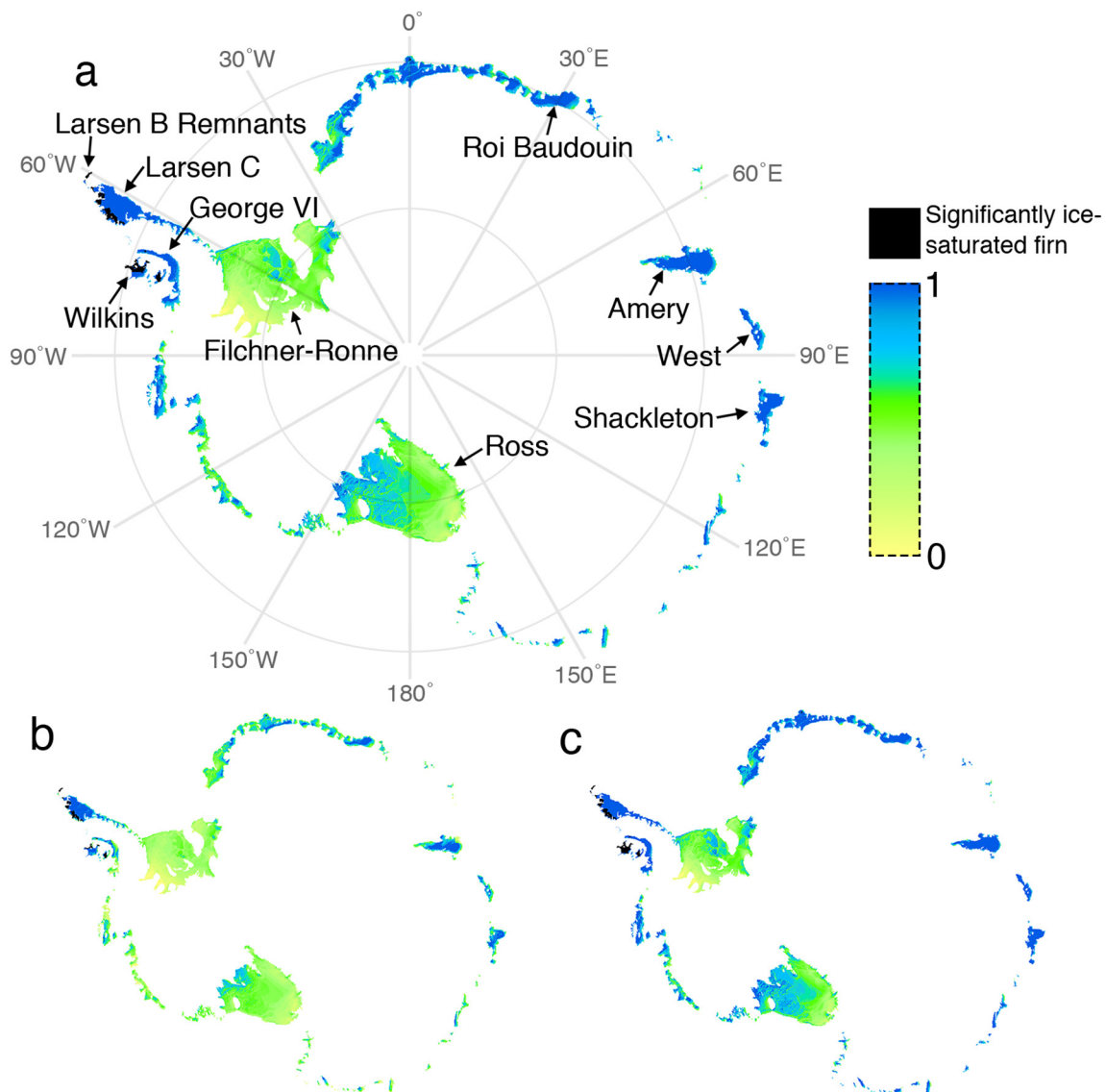


Fig. 5. Vulnerability index results. a) Vulnerability index derived from the QuikSCAT data divided into surface mass balance categories as plotted in Fig. 4. Labeled shelves are mentioned in the text. b) Vulnerability index minus two standard deviations. c) Vulnerability index plus two standard deviations.

the Monte Carlo simulations for each pixel. The lower and upper bounds for the vulnerability index are shown in Fig. 5b–c, respectively. The spread between the upper and lower bounds was typically between 5% and 40% of the calculated index values (Fig. 5a). Because we could not explicitly address every variable that would add scatter to the data (e.g. crevassing, mixed pixels, and sastrugi, as discussed in Section 4), this statistical technique gives us some quantification of how much outlying values are likely to be affecting our index. Overall, the results shown Fig. 5 indicate that the scatter in the data has relatively little impact on the patterns of vulnerability presented by our index.

6. Discussion of vulnerability index results

The results of the vulnerability index are shown in Fig. 5a. Antarctica's largest ice shelves, the Ross and the Filchner-Ronne, plot relatively low on the vulnerability index, and thus we infer that they are in no immediate danger of surface-melt-induced collapse. Some shelves, such as the Amery (Fig. 7a), West, and Shackleton, have areas with very high vulnerability indices. These areas experience localized high annual melt rates, in many cases due to persistent, warm föhn or katabatic winds that travel down large slopes near the grounding line (Cape et al.,

2015; Lenaerts et al., 2016). Some areas on the Roi Baudouin Ice Shelf (Fig. 7b), which also experiences high melt rates due to katabatic winds (Lenaerts et al., 2016) may show artificially low vulnerability due to the presence of liquid water in some measurements, which causes very large decreases in backscatter.

The areas identified as currently most vulnerable to collapse, plotting above the specular reflection threshold, are found on the Antarctic Peninsula. These include remnants of the Larsen B, parts of the Larsen C, and much of the Wilkins and Bach Ice Shelves. These areas are interpreted to have the potential to support melt ponding given the right future climatic conditions; however, not all these areas currently exhibit melt ponding. Similarly, some areas that currently support melt ponds, such as the grounding line region of the Roi Baudouin Ice Shelf in Queen Maud Land, fall below the “significantly ice-saturated” threshold. These plot at very high values on the index, and are likely to contain a large proportion of smaller ice lenses that do not cause strong specular reflections but still impede downward meltwater percolation.

We checked the validity of our index in two ways. First, we generated a lower-resolution mapping of vulnerability using ASCAT data and temporally coincident melt days data generated from a passive microwave record (Fig. 6) (Picard and Fily, 2006). The mapped

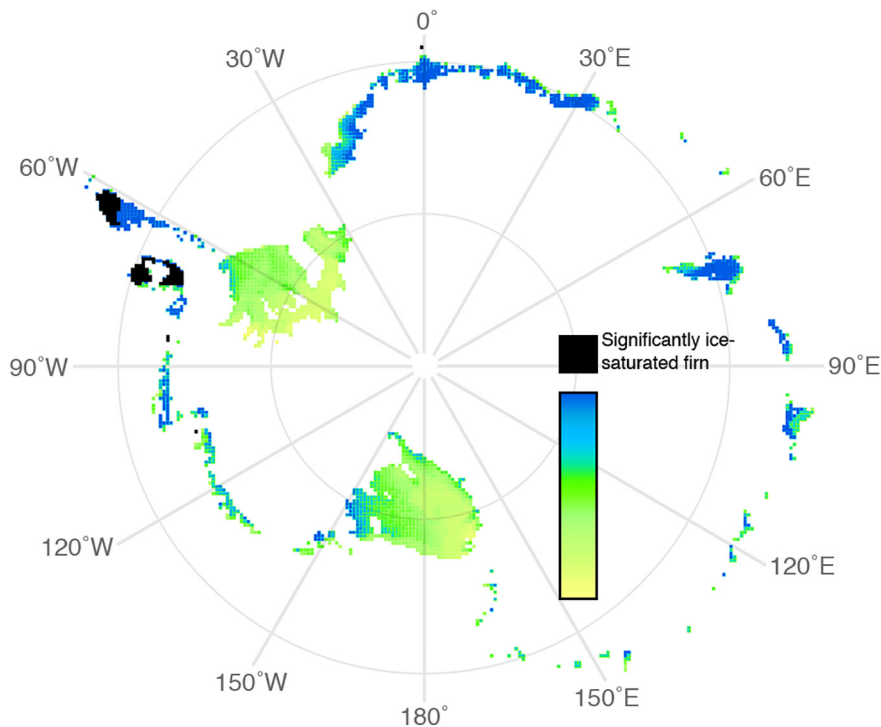


Fig. 6. Vulnerability index derived from ASCAT data as shown in black in Fig. 3d.

vulnerability index is nearly identical to the index derived from QuikSCAT (Fig. 5a), indicating that our approach yields consistent results. Small differences between the indices may represent differences in the penetration depth of the sensors used, the effects of widely differing resolutions, or real firn layer evolution that occurred between the different time periods represented. Second, we compared the patterns in our results to those of Holland et al. (2011), who used an independent method relying on radio-echo sounding to estimate the air content of the firn on the Larsen C Ice Shelf. As shown in Fig. 7c–d, the qualitative patterns in our vulnerability index match closely with the Holland et al. (2011) results, showing the highest vulnerability near the grounding line to the northwest where firn air thickness is lowest, and moving towards lower vulnerabilities towards the southeast corner as firn air content increases. A pixel-by-pixel correlation between the two assessments yields a Spearman's rho of -0.56 . After accounting for spatial autocorrelation using a K-nearest neighbors approach, we found a significant p-value of 0.0000. More recent in situ data has documented extensive, thick ice lenses in some of the locations we have marked as significantly ice-saturated (Hubbard et al., 2016), and Holland et al. (2015) documented a continuing loss of firn air thickness in the same regions.

The map also suggests another important factor in the likelihood of an ice shelf to be affected by surface-melt-induced instability: ice shelf geometry. Some studies indicate that ice shelf flow is only stable in certain configurations, with a “compressive arch” at the ice front keeping the ice flow in balance (Doake et al., 1998; Fürst et al., 2016). Breaching of the compressive arch and runaway disintegration due to capsizing ice blocks (MacAyeal et al., 2003) are possible in part due to ice shelf geometry. The Larsen B, for example, flowed freely in a relatively wide embayment with few pinning points to stabilize the middle of the shelf before its collapse. An ice shelf like the George VI is unlikely to be as vulnerable to a hydrofracture collapse mechanism because it is tightly confined by its embayment (Scambos et al., 2000; Kuipers Munneke et al., 2014). And although the Wilkins Ice Shelf has a widely saturated firn layer according to our index and many visible surface melt ponds, its large number of pinning points could help stabilize the shelf. The advanced position of the Larsen C Ice Shelf on the

vulnerability index and its relatively unconfined geometry make it a critical shelf to monitor in the future.

7. Conclusions

The relationship between active microwave backscatter and average annual melt days reveals important information about the evolution of firn on ice shelves. A transect from Greenland, where snow facies are well-documented, compared with field data, demonstrates that backscatter increases with increasing mean annual melt days until specular reflections due to large, continuous ice lenses in the firn layer at high melt days causes the backscatter to decrease. Although less obvious because of large amounts of scatter in the data, this relationship is nonetheless also present in the mean backscatter relationship plotted from all Antarctic ice shelves. The scatter in the raw data is primarily explained by differences in surface mass balance and its effects on the air content of the firn within areas that would be classified as the same snow facies. The consistency of the relationship across sensors and time periods allows us to use it as the basis for a vulnerability index, identifying which ice shelves are currently or may soon be vulnerable to hydrofracture. Several ice shelves on the Antarctic Peninsula have areas of significantly ice-saturated firn layers. The likelihood of an ice shelf with an ice-saturated firn layer to collapse is modulated by the geometry of the ice shelf.

Acknowledgments

The completion of this study was supported by NASA through a NASA Earth Science Student Fellowship (NNX14AK82H). Greenland field data were collected with the support of a NASA Cryospheric Sciences award (NNX10AC76G). The authors declare no financial conflicts of interest in the completion of the manuscript. We would like to thank P. Holland for providing data and helpful comments in the preparation of this manuscript, and A. Crawford for assistance with statistical analyses. All data are available through the Brigham Young University Microwave Earth Remote Sensing Laboratory Scatterometer Climate Record Pathfinder (<http://www.scp.byu.edu>) and by

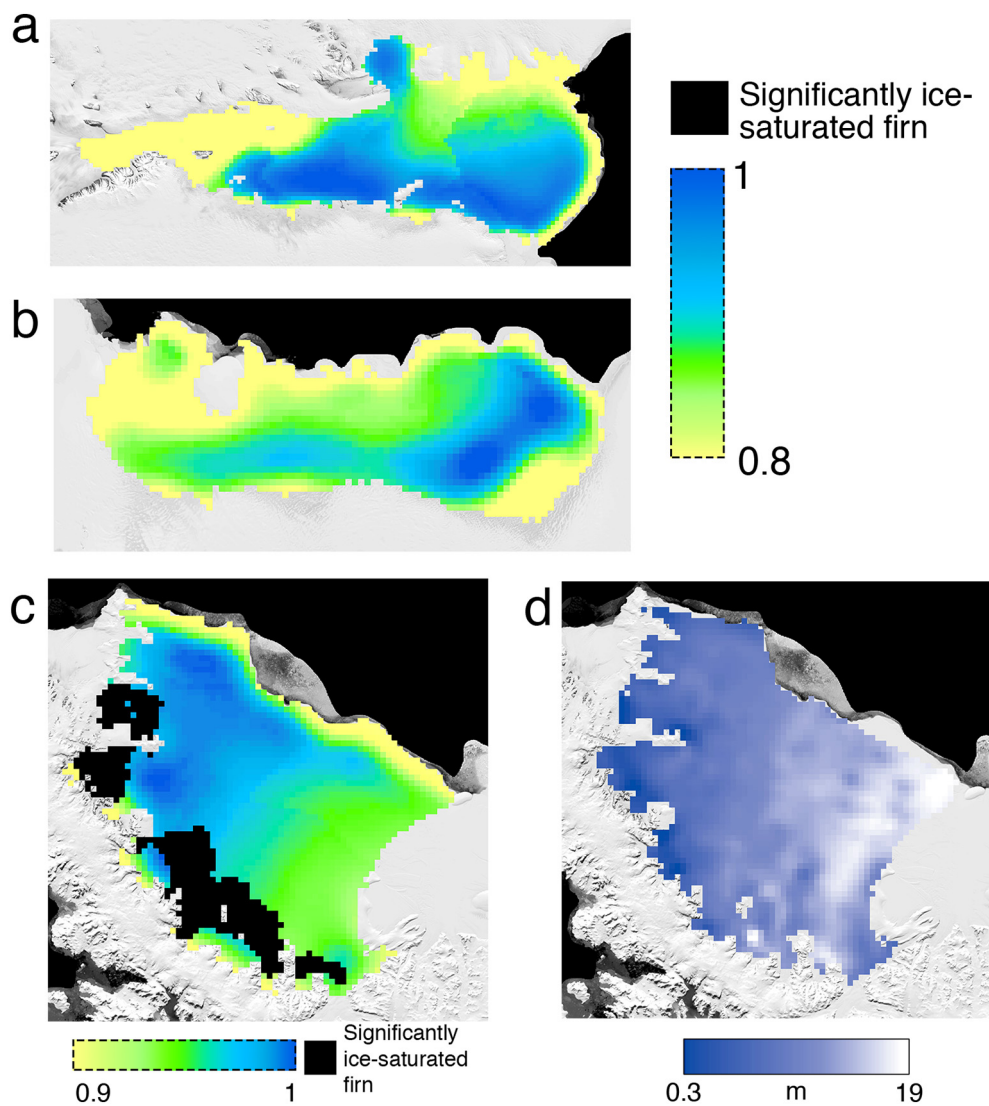


Fig. 7. Vulnerability index details. a–b) Vulnerability index for the Amery and Roi Baudouin Ice Shelves, which are labeled in Fig. 5. The index for both shelves is plotted using the colorbar to the right. c) Vulnerability index for the Larsen C ice shelf on the Antarctic Peninsula. d) Firn air thickness on the Larsen C ice shelf from Holland et al. (2011).

contacting the authors directly.

Appendix A. Supplementary data

Supplementary data to this article can be found online at <https://doi.org/10.1016/j.rse.2018.03.025>.

References

- Benson, C.S., 1962. Stratigraphic studies in the snow and firn of the Greenland ice sheet. Res. Rep. 70 (93 pp., U. S. Army Cold Reg. Res. and Eng. Lab., Hanover, N. H. (Reprinted and updated in 1996.)) (1962).
- Berthier, E., Scambos, T.A., Shuman, C.A., 2012. Mass loss of Larsen B tributary glaciers (Antarctic Peninsula) unabated since 2002. *Geophys. Res. Lett.* 39 (13). <http://dx.doi.org/10.1029/2012GL051755>. (L13501).
- Bingham, A.W., Drinkwater, M.R., 2000. Recent changes in the microwave scattering properties of the Antarctic ice sheet. *IEEE Trans. Geosci. Remote Sens.* 38 (4), 1810–1820.
- Braithwaite, R.J., Laternser, M., Pfeffer, W.T., 1994. Variations of near-surface firn density in the lower accumulation area of the Greenland ice sheet, Pákitsoq, West Greenland. *J. Glaciol.* 40 (136), 477–485. <http://dx.doi.org/10.3198/1994JoG40-136-477-485>.
- Cape, M.R., Vernet, M., Skvarca, P., Marinsek, S., Scambos, T., Domack, E., 2015. Foehn winds link climate-driven warming to ice shelf evolution in Antarctica. *J. Geophys. Res. Atmos.* 120 (21), 11,037–11,057. <http://dx.doi.org/10.1002/2015JD023465>.
- Carsey, F.D., 1992. Microwave remote sensing of sea ice. In: *American Geophysical Union, Geophysical Monograph Series*. 68 (Washington DC).
- Doake, C.S.M., Corr, H.F.J., Rott, H., Skvarca, P., Young, N.W., 1998. Breakup and conditions for stability of the northern Larsen Ice Shelf, Antarctica. *Nature* 391 (6669), 778–780. <http://dx.doi.org/10.1038/35832>.
- Fahnestock, M., Bindschadler, R., Kwok, R., Jezek, K.C., 1993. Greenland ice sheet surface properties and ice dynamics from ERS-1 SAR imagery. *Science* 262 (5139), 1530–1534. <http://dx.doi.org/10.1126/science.262.5139.1530>.
- Fraser, A.D., Young, N.W., Adams, N., 2014. Comparison of microwave backscatter anisotropy parameterizations of the Antarctic ice sheet using ASCAT. *Trans. Geosci. Remote Sens.* 52 (3), 1583–1595. <http://dx.doi.org/10.1109/TGRS.2013.2252621>.
- Forster, R.R., Box, J.E., van den Broeke, M.R., Miege, C., Burgess, E.W., van Angelen, J.H., Leanarts, J.T.M., Koenig, L.S., Paden, J., Lewis, C., Gogineni, S.P., Leuschen, C., McConnell, J.R., 2013. Extensive liquid meltwater storage in firn within the Greenland ice sheet. *Nat. Geosci.* 7 (2), 95–98. <http://dx.doi.org/10.1038/ngeo2043>.
- Fürst, J.J., Durand, G., Gillet-Chaulet, F., Tavaré, L., Rankl, M., Braun, M., Gagliardini, O., 2016. The safety band of Antarctic ice shelves. *Nat. Clim. Chang.* 6, 479–482. <http://dx.doi.org/10.1038/nclimate2912>.
- Haas, C., Thomas, D.N., Bareiss, J., 2001. Surface properties and processes of perennial Antarctic sea ice in summer. *J. Glaciol.* 47 (159), 613–625. <http://dx.doi.org/10.3189/172756501781831864>.
- Hall, D.K., Williams, R.S., Barton, J.S., Sigurdsson, O., Smith, L.C., Garvin, J.B., 2000. Evaluation of remote-sensing techniques to measure decadal-scale changes of Hofsjökull ice cap, Iceland. *J. Glaciol.* 46 (154), 375–388. <http://dx.doi.org/10.3189/172756500781833061>.
- Haran, T., Bohlander, J., Scambos, T., Painter, T., Fahnestock, M., 2014. MODIS Mosaic of Antarctica 2008–2009 (MOA2009) Image Map. Boulder, Colorado USA. NSIDC: National Snow and Ice Data Center. <https://doi.org/10.7265/N5KP8037> (accessed 2016).
- Hicks, B.R., Long, D.G., 2011. Inferring Greenland melt and refreeze severity from SeaWinds scatterometer data. *Int. J. Remote Sens.* 32 (23), 8053–8080. <http://dx.doi.org/10.1080/01431161.2010.532174>.

- Holland, P.R., Corr, H.F.J., Pritchard, H.D., Vaughan, D.G., Arthern, R.J., Jenkins, A., Tedesco, M., 2011. The air content of Larsen Ice Shelf. *Geophys. Res. Lett.* 38 (10). <http://dx.doi.org/10.1029/2011GL047245>. (L10503).
- Holland, P.R., Brisbourne, A., Corr, H.F.J., McGrath, D., Purdon, K., Paden, J., Fricker, H.A., Paolo, F.S., Fleming, A.H., 2015. Oceanic and atmospheric forcing of Larsen C ice-shelf thinning. *Cryosphere* 9 (3), 1005–1024. <http://dx.doi.org/10.5194/tc-9-1005-2015>.
- Hubbard, B., Luckman, A., Ashmore, D.W., Bevan, S., Kulesa, B., Kuipers Munneke, P., Philippe, M., Jansen, D., Booth, A., Sevestre, H., Tison, J.L., O'Leary, M., Rutt, I., 2016. Massive subsurface ice formed by refreezing of ice-shelf melt ponds. *Nat. Commun.* 7, 1–6. <http://dx.doi.org/10.1038/ncomms11897>.
- Hughes, T., 1983. On the disintegration of ice shelves: the role of fracture. *J. Glaciol.* 29 (101), 98–117. <http://dx.doi.org/10.1017/S0022143000005177>.
- Humphrey, N.F., Harper, J.T., Pfeffer, W.T., 2012. Thermal tracking of meltwater retention in Greenland's accumulation area. *J. Geophys. Res. Earth Surf.* 117 (F1), F01010. <http://dx.doi.org/10.1029/2011JF002083>.
- Jezek, K.C., Drinkwater, M.R., Crawford, J.P., Bindschadler, R., Kwok, R., 1993. Analysis of synthetic aperture radar data collected over the southwestern Greenland ice sheet. *J. Glaciol.* 39 (131), 119–132. <http://dx.doi.org/10.3198/1993JoG39-131-119-132>.
- Jezek, K.C., Gogineni, P., Shanableh, M., 1994. Radar measurements of melt zones on the Greenland ice sheet. *Geophys. Res. Lett.* 21 (1), 33–36. <http://dx.doi.org/10.1029/93GL03377>.
- Kuipers Munneke, P., Ligtenberg, S.R.M., Van Den Broeke, M.R., Vaughan, D.G., 2014. Firm air depletion as a precursor of Antarctic ice-shelf collapse. *J. Glaciol.* 60 (220), 205–214. <http://dx.doi.org/10.3189/2014JoG13J183>.
- Lenaerts, J., Lhermitte, S., Drews, R., Ligtenberg, S.R.M., Berger, S., Helm, V., Smeets, C.J.P.P., van den Broeke, M.R., van de Berg, W.J., van Meijgaard, E., Eijkelboom, M., Eisen, O., Pattyn, F., 2016. Meltwater produced by wind-albedo interaction stored in an East Antarctic ice shelf. *Nat. Clim. Chang.* 7, 58–62. <http://dx.doi.org/10.1038/nclimate3180>.
- Long, D.G., Drinkwater, M.R., 1994. Greenland ice-sheet surface properties observed by the Seasat-A scatterometer at enhanced resolution. *J. Glaciol.* 40 (135), 213–230. <http://dx.doi.org/10.3198/1994JoG40-135-213-230>.
- Long, D.G., Hardin, P.J., Whiting, P.T., 1993. Resolution enhancement of spaceborne scatterometer data. *IEEE Trans. Geosci. Remote Sens.* 31 (3), 700–715. <http://dx.doi.org/10.1109/36.225536>.
- MacAyeal, D.R., Scambos, T.A., Hulbe, C.L., Fahnestock, M.A., 2003. Catastrophic ice-shelf break-up by an ice-shelf-fragment-capsize mechanism. *J. Glaciol.* 49 (164), 22–36. <http://dx.doi.org/10.3189/172756503781830863>.
- Machguth, H., MacFerrin, M., van As, D., Box, J.E., Charalampidis, C., Colgan, W., Fausto, R.S., Meijer, H.A.J., Mosley-Thompson, E., van de Wal, R.S.W., 2016. Greenland meltwater storage in firm limited by near-surface ice formation. *Nat. Clim. Chang.* 6 (4), 390–393. <http://dx.doi.org/10.1038/nclimate2899>.
- Mote, Thomas L., 2014. MEASURES Greenland Surface Melt Daily 25 km EASE-Grid 2.0, [2004–2013]. Boulder, Colorado USA: NASA DAAC at the National Snow and Ice Data Center. <http://dx.doi.org/10.5067/MEASURES/CRYOSPHERE/nsidc-0533.001>.
- Partington, K.C., 1998. Discrimination of glacier facies using multi-temporal SAR data. *J. Glaciol.* 44 (146), 42–53. <http://dx.doi.org/10.3198/1998JoG44-146-42-53>.
- Pfeffer, W.T., Meier, M.F., Illangasekare, T.H., 1991. Retention of Greenland runoff by refreezing: implications for projected future sea level change. *J. Geophys. Res.* 96 (C12), 22117–22124. <http://dx.doi.org/10.1029/91JC02502>.
- Picard, G., Fily, M., 2006. Surface melting observations in Antarctica by microwave radiometers: correcting 26-year time series from changes in acquisition hours. *Remote Sens. Environ.* 104 (3), 325–336. <http://dx.doi.org/10.1016/j.rse.2006.05.010>.
- Rignot, E., Echelmeyer, K., Krabill, W., 2001. Penetration depth of interferometric synthetic-aperture radar signals in snow and ice. *Geophys. Res. Lett.* 28 (18), 3501–3504.
- Rott, H., Sturm, K., Miller, H., 1993. Active and passive microwave signatures of Antarctic firm by means of field measurements and satellite data. *Ann. Glaciol.* 17, 337–343. <http://dx.doi.org/10.3198/1993AoG17-1-337-343>.
- Rott, H., Skvarca, P., Nagler, T., 1996. Rapid collapse of northern Larsen Ice Shelf, Antarctica. *Science* 271 (5250), 788–792. <http://dx.doi.org/10.1126/science.271.5250.788>.
- Scambos, T.A., Hulbe, C., Fahnestock, M., Bohlander, J., 2000. The link between climate warming and break-up of ice shelves in the Antarctic Peninsula. *J. Glaciol.* 46 (154), 516–530. <http://dx.doi.org/10.3189/172756500781833043>.
- Scambos, T., Hulbe, C., Fahnestock, M., 2003. Climate-induced ice shelf disintegration in the Antarctic Peninsula. In: Domack, E., Leventer, A., Burnett, A., Bindschadler, R., Convey, P., Kirby, M. (Eds.), *Antarctic Peninsula Climate Variability: Historical and Paleoenvironmental Perspectives*. American Geophysical Union, Washington, D. C. <http://dx.doi.org/10.1029/AR079p0079>.
- Scambos, T.A., Haran, T.M., Fahnestock, M.A., Painter, T.H., Bohlander, J., 2007. MODIS-based mosaic of Antarctica (MOA) data sets: continent-wide surface morphology and snow grain size. *Remote Sens. Environ.* 111 (2–3), 242–257. <http://dx.doi.org/10.1016/j.rse.2006.12.020>.
- Trusel, L.D., Frey, K.E., Das, S.B., 2012. Antarctic surface melting dynamics: enhanced perspectives from radar scatterometer data. *J. Geophys. Res.* 117 (F02023), 1–15. <http://dx.doi.org/10.1029/2011JF002126>.
- Van Wessem, J.M., Reijmer, C.H., Morlighem, M., Mougnot, J., Medley, B., Joughin, I., Wouters, B., Depoorter, M.A., Bamber, J.L., Lenaerts, J.T.M., van de Berg, W.J., van den Broeke, M.R., van Meijgaard, E., 2014. Improved representation of East Antarctic surface mass balance in a regional atmospheric climate model. *J. Glaciol.* 60 (222), 761–770. <http://dx.doi.org/10.3189/2014JoG14J051>.
- Willmes, S., Haas, C., Nicolaus, M., 2011. High radar-backscatter regions on Antarctic sea-ice and their relation to sea-ice and snow properties and meteorological conditions. *Int. J. Remote Sens.* 32 (14), 3967–3984. <http://dx.doi.org/10.1080/01431161003801344>.